Convective Transition Statistics over Tropical Oceans for Climate Model Diagnostics: Observational Baseline

YI-HUNG KUO, KATHLEEN A. SCHIRO, AND J. DAVID NEELIN

Department of Atmospheric and Oceanic Sciences, University of California, Los Angeles, Los Angeles, California

(Manuscript received 22 September 2017, in final form 21 February 2018)

ABSTRACT

Convective transition statistics, which describe the relation between column-integrated water vapor (CWV) and precipitation, are compiled over tropical oceans using satellite and ARM site measurements to quantify the temperature and resolution dependence of the precipitation–CWV relation at fast time scales relevant to convection. At these time scales, and for precipitation especially, uncertainties associated with observational systems must be addressed by examining features with a variety of instrumentation and identifying robust behaviors versus instrument sensitivity at high rain rates. Here the sharp pickup in precipitation as CWV exceeds a certain critical threshold is found to be insensitive to spatial resolution, with convective onset occurring at higher CWV but at lower column relative humidity as bulk tropospheric temperature increases. Mean tropospheric temperature profiles conditioned on precipitation show vertically coherent structure across a wide range of temperature, reaffirming the use of a bulk temperature measure in defining the convective transition statistics. The joint probability distribution of CWV and precipitation develops a peak probability at low precipitation for CWV above critical, with rapidly decreasing probability of high precipitation below and near critical, and exhibits systematic changes under spatial averaging. The precipitation pickup with CWV is reasonably insensitive to time averaging up to several hours but is smoothed at daily time scales. This work demonstrates that CWV relative to critical serves as an effective predictor of precipitation with only minor geographic variations in the tropics, quantifies precipitation-related statistics subject to different spatial–temporal resolution, and provides a baseline for model comparison to apply these statistics as observational constraints on precipitation processes.

1. Introduction

Despite the ongoing improvement of weather and climate modeling in recent decades in terms of model resolution and number of simulated processes, convective parameterization remains a major contributor to the uncertainty of future projection (Sanderson 2011; Rowell 2012; Yokohata et al. 2012; Sherwood et al. 2014), and systematic biases in precipitation and clouds persist. A nonexhaustive list of persistent biases includes the double ITCZ bias (Mapes and Neale 2011; Hirota et al. 2014), insensitivity of precipitation to environment humidity (Oueslati and Bellon 2013), low bias in tropospheric humidity (Gonzalez and Jiang 2017), failing to capture the amplitude and propagation of MJO (Kim et al. 2014; Jiang et al. 2016; Jiang 2017), unrealistic statistics and surface storm tracks for tropical cyclones (Booth et al. 2017), and incorrect precipitation diurnal cycle over land (Covey et al. 2016). These biases also impact model diagnosis for short-term forecasting purposes, since models adopted for weather forecasting or reanalysis share common components with climate models.

Many conventional diagnostics for climate models emphasize comparisons against long-term climatology or variability at different time scales, and the model performance examined by these metrics is affected by multiple factors. While sensitivity experiments with respect to such metrics are useful in identifying important processes (Benedict et al. 2013, 2014; Boyle et al. 2015; Bernstein and Neelin 2016; Langenbrunner and Neelin 2017), the contribution of certain processes can be difficult to isolate, making constraining model performance challenging. As such, there is an emerging need for diagnostics targeting processes and focusing on the most relevant time scales. This study presents an example of such process-oriented diagnostics—the convective

Supplemental information related to this paper is available at the Journals Online website: https://doi.org/10.1175/JAS-D-17-0287.s1.

Corresponding author: Yi-Hung Kuo, yhkuo@atmos.ucla.edu

DOI: 10.1175/JAS-D-17-0287.1

transition statistics—that focus on the fast-time-scale deep convection in the tropics.

The sensitivity of moist convection to lower-free-tropospheric humidity had been suggested by the analysis of TOGA COARE and operational sounding data for the tropical western Pacific (Brown and Zhang 1997; Sherwood and Wahrlich 1999; Parsons et al. 2000) and was subsequently affirmed by numerical experiments (Tompkins 2001; Redelsperger et al. 2002; Ridout 2002; Derbyshire et al. 2004). Later observational and modeling studies pointed to the importance of organized convective systems in determining the environment moisture field (Tao and Moncrieff 2009; Yano et al. 2012; Moncrieff et al. 2017). Bretherton et al. (2004) documented an empirical relationship between the column relative humidity (CRH) and precipitation over tropical oceans at daily and monthly time scales in SSM/I satellite retrievals (see also Rushley et al. 2018). Based on the analysis of the same satellite observations at fast time scales, Peters and Neelin (2006) noted a sharp increase in precipitation as the column-integrated water vapor (CWV) exceeded a certain threshold and, using the analogy to associated behavior in continuous phase transitions, showed consistent relations among a set of statistics, including probability and variance of precipitation, and the distribution of CWV for precipitating events. Subsequent studies have examined the dependence on tropospheric temperature (Neelin et al. 2009) and how the statistics can be reproduced by simple stochastic models (Stechmann and Neelin 2011, 2014). The plume buoyancy calculations based on ground-based measurements at tropical ARM sites (Holloway and Neelin 2009; Schiro et al. 2016) and the NCAR CAM5 simulations (Sahany et al. 2012; Kuo et al. 2017) have demonstrated that entrainment is instrumental in explaining the observed precipitation–CWV relation and that the relation is qualitatively robust over land and ocean. These convective transition statistics characterize the dependence of tropical convection on bulk measures of the water vapor–temperature environment.

The robust rapid increase in conditionally averaged precipitation and conditional probability of precipitation as CWV exceeds a certain threshold (the ''pickup of precipitation'') derived from the tropical ARM sites have been used to constrain the entrainment parameter in the NCAR CESM (Kuo et al. 2017). Given that precipitation-related statistics are sensitive to resolution (Chen and Dai 2018; Klingaman et al. 2017), to allow for a more quantitative comparison to model output subject to varying spatial resolution and temporal frequency, the dependence of the convective transition statistics on spatial–temporal resolution must be quantified. Moreover, the robustness to instrumentation, especially at high rain rate, should be addressed to ensure the reliability of such diagnostics. The purposes of this study are to quantify the resolution dependence and robustness of the statistics, to provide an observational baseline for model comparison, and to expand the set of related properties that can be understood within this framework.

This manuscript is organized as follows. Section 2 describes the datasets analyzed here. The basic convective transition statistics, which build on those introduced in previous work (e.g., Peters and Neelin 2006; Neelin et al. 2008), are presented in section 3 with the following additions: using newer datasets, assessing the spatial resolution dependence of the statistics, testing the robustness to instrumentation, and evaluating sensitivity to the choice of bulk measure of tropospheric temperature. Sections 4–6 explore new statistics characterizing the convective transition. Section 4 examines the geographic variations, or the lack thereof, of the effectiveness of CWV relative to critical as a predictor of precipitation and the associated dependences on spatial–temporal resolution. The sensitivity of the statistics to time averaging is discussed in section 5. The joint probability density function (PDF) of CWV and precipitation, and its dependence on spatial resolution and instrumentation, are shown in section 6. Finally, section 7 summarizes the properties of convective transition statistics and briefly discusses their potential as diagnostic tools.

2. Datasets

Compiling the convective transition statistics requires CWV, precipitation rate P, column-integrated saturation humidity $\widehat{q_{\rm sat}}$ $\{\equiv\int q_{\rm sat}[T(p), p]\,dp/g$; here $q_{\rm sat}[T(p), p]$ is the saturation specific humidity with respect to liquid water as a function of temperature $T(p)$ and pressure $p\}$, and mass-weighted column-averaged temperature $\hat{T}$.

The primary source of CWV and P here is the TRMM Microwave Imager (TMI) retrieval products processed by Remote Sensing Systems (RSS; algorithm v7.1, TMIv7.1 hereafter; Wentz et al. 2015). The retrieved values include gridded ($0.25° \times 0.25°$) snapshots of CWV (0.3 mm) and P ($0.1\,{\rm mm\,h^{-1}}$) over ocean, with no data available over land. The TRMM Precipitation Radar (PR) 2A25 (v7; TRMM 2011a) and TRMM 3B42 (v7; TRMM 2011b) Rainfall Rate products are used for comparison. The 2A25 data provide snapshots of P with resolution ~5 km × 5 km, and 3B42 provides gridded ($0.25° \times 0.25°$) P every 3 h. Note that 3B42 is a merged product; as such, most values should be interpreted as instantaneous, since P is observed during a specific 3-h window rather than a computed 3-hourly mean. Here, the TMIv7.1, 2A25, and 3B42 data for 1 June 2002–31 May 2014 are used.

The Microwave Radiometer (MWR) CWV and rain gauge P measurements collected from the DOE ARM sites at Nauru (0°31′S, 166°54′E) for 1999–2008 (Gaustad and Riihimaki 1998; Holdridge and Kyrouac 1998) and at Manus (2°3′S, 147°25′E) for 1998–2010 (Gaustad and Riihimaki 1996; Holdridge and Kyrouac 1997) in the tropical western Pacific (both with optical rain gauge) and at the ARM Mobile Facility near Manaus (3°7′S, 60°1′W) for 10 January 2014–20 October 2015 (Koontz et al. 2015; Gaustad and Riihimaki 2015) during the Green Ocean Amazon (GOAmazon) campaign (with acoustic rain gauge) are also used to study the sensitivity of the statistics to instrumentation and time averaging.

For column-integrated/averaged $\widehat{q_{\rm sat}}$ and $\hat{T}$, with the column being defined as 1000–200 hPa, the 6-hourly 2.5° NCEP–DOE Reanalysis-2 (Kanamitsu et al. 2002) temperature is adopted with necessary interpolation. Since the spatial and temporal autocorrelation scales of temperature are expected to be large in the tropics, the interpolation is justified. To avoid potentially erroneous temperature values from spatial interpolation (e.g., around the Andes and New Guinea), data in the 2.5° neighborhood of land pixels are excluded for some of the presented statistics.

Note that the CWV datasets often do not record a CWV value in the presence of precipitation, and thus gap filling is required to reconstruct missing data (see section S1 in the supplementary material). For algorithm choices used for the TMIv7.1 data, the probability of missing CWV depends primarily on P, with the probability increasing from 0 to 1 almost linearly as P increases from 2 to 9 mm h^{-1}. This even affects the tropical-mean precipitation; for example, the annual-mean precipitation over tropical oceans (20°S–20°N) is reduced from 3.1 to 2.1 mm day^{-1} by excluding precipitation without valid CWV retrievals. Therefore, it is necessary to gap-fill these missing CWV values; otherwise, the information comprising the desired statistics would be systematically distorted. Here the default is to simply fill the missing values using the available CWV value at the geographically nearest pixel. The sensitivity of the presented statistics to the gap filling are included in section S4 of the supplemental material (Figs. S7–S11). Similarly, the raw CWV time series from the tropical ARM site MWR measurements are recorded every 20 s, but exhibit gaps because of the ''wet window'' effect. Gaps shorter than 6 h are filled using linear interpolation as described in Schiro et al. (2016). The gap-filled time series are then used to calculate the mean time series at lower temporal frequencies (e.g., 5-min or hourly average). Precipitation observations are available in the CWV gaps and do not have to be interpolated.

Additionally, satellite CWV retrievals processed by RSS (including TMIv7.1) have a 75-mm cap set by the algorithm. While CWV rarely exceeds 75 mm, operational soundings occasionally record such events; for example, weather stations in Ishigakijima (24°20′N, 124°10′E; station 47918) and Taipei (25°02′N, 121°31′E; station 58968) recorded 80.03 and 82.54 mm at 0000 and 1200 UTC, respectively, on 21 August 2013 under the influence of Typhoon Trami (data from University of Wyoming 2017). This serves as a reminder of the imperfect observational systems, and one must keep in mind the uncertainties when applying the presented statistics for model diagnosis.

3. Dependence of precipitation–CWV relation on tropospheric temperature and spatial resolution

a. *Basic features of convective transition statistics*

Figure 1 shows the basic convective transition statistics, including the precipitation rate (Fig. 1a), probability of precipitation (Fig. 1b; $P > 1.05$ mm h^{-1}), PDFs of all events (Fig. 1c), and precipitating events (Fig. 1d) conditioned on CWV and $\widehat{q_{\rm sat}}$ for the tropical western Pacific, along with results for other tropical ocean basins (Figs. 1e–p). Here the statistics are compiled at 0.25° (colored markers) and 0.5° (dots), using $\widehat{q_{\rm sat}}$ as the bulk tropospheric temperature. The standard errors associated with the conditionally averaged precipitation (conditional precipitation hereinafter) at 0.25° are smaller than the marker size, because of the large number of counts in each bin (on the order of 10^3–10^5), and thus are omitted. To exclude light precipitation and focus on deep convective events, a threshold of 1.05 mm h^{-1} defining precipitating events is chosen, with a natural offset 0.05 since the TMIv7.1 precipitation is discretized by 0.1 mm h^{-1} units. Note that the PDFs of all events (e.g., Fig. 1c)—that is, PDFs of CWV—are calculated from the joint PDF of CWV and $\widehat{q_{\rm sat}}$, normalized for each basin, by treating CWV as a continuous variable and $\widehat{q_{\rm sat}}$ discretely. These PDFs, when multiplied by the corresponding conditional probabilities (Fig. 1b), give the PDFs for precipitating events (Fig. 1d). The jumps at 75 mm for the PDFs result from the CWV cap set by the retrieval algorithm. For sensitivity to gap filling, see section S4 (Figs. S7–S11).

For each $\widehat{q_{\rm sat}}$, the conditional precipitation and probability (Fig. 1; first and second columns) pick up sharply as CWV exceeds a certain threshold, referred to as the ''critical CWV'' or w_c (defined in section 3b), around which the PDF of precipitating events (fourth column) peaks. The precipitation pickup occurs at higher CWV for higher $\widehat{q_{\rm sat}}$, that is, w_c is increasing with $\widehat{q_{\rm sat}}$. The conditional probability would decrease with an increase in the threshold that defines precipitating events; that is, the probability curves would move toward higher CWV. The spacing between pickup curves (for conditional precipitation and probability) suggests that the behavior for $\widehat{q_{\rm sat}}$ bins ≥61 mm (>85% of total occurrence over

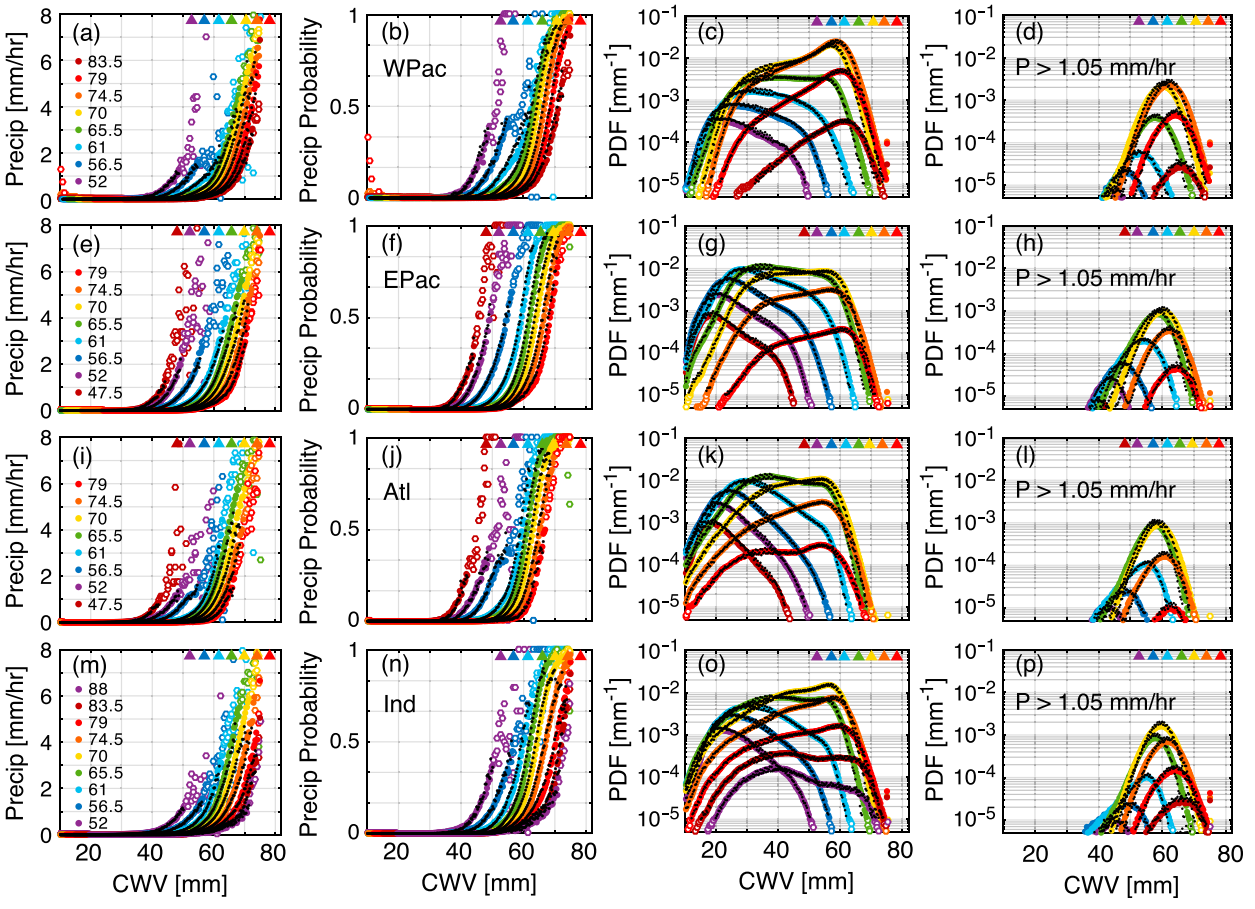

FIG. 1. (a) Conditionally averaged precipitation rate, (b) conditional probability of precipitation, (c) probability density function of all events, and (d) precipitating events only as a function of CWV and $\widehat{q_{\rm sat}}$ (mm) for the tropical (20°S–20°N) western Pacific. (e)–(p) As in (a)–(d), but for the (e)–(h) tropical eastern Pacific, (i)–(l) Atlantic, and (m)–(p) Indian Ocean. Results are shown using TMIv7.1 data and Reanalysis-2 temperature compiled at 0.25° (colored markers) and 0.5° (dots). Underpopulated bins at 0.25° (PDF $< 10^{-5}$) are indicated by open circles, and those for 0.5° are omitted. Triangles represent the corresponding $\widehat{q_{\rm sat}}$ values. Here, precipitating events are defined by $P > 1.05$ mm h^{-1}. The CWV data is gap-filled using nearest available values, and data from pixels within 2.5° of land are excluded to avoid potentially erroneous temperature values arising from spatial interpolation. The standard errors associated with the conditional precipitation are smaller than the marker size and are omitted. The corresponding statistics compiled using $\hat{T}$ as the bulk tropospheric temperature measure are plotted in Fig. S4.

tropical oceans) is slightly different from that in lower $\widehat{q_{\rm sat}}$ bins. Inspection of the geographical distribution of $\widehat{q_{\rm sat}}$ occurrence suggests that low-$\widehat{q_{\rm sat}}$ events are due mostly to systems originating from the extratropics (section S6).

The observed sharp increase in precipitation as CWV exceeds critical has been explained by entraining plume calculations, through which the deep convective conditional instability can be estimated. As previously demonstrated (Holloway and Neelin 2009; Schiro et al. 2016; Kuo et al. 2017), CWV serves as a measure of the impact of environment moisture on plume buoyancy, and hence the instability, through the effects of mixing, as indicated by the precipitation pickup. The dependence of w_c on $\widehat{q_{\rm sat}}$ can be explained through a similar approach (Sahany et al. 2012).

In Fig. 1, the dots (0.5°) match the colored markers (0.25°) in the first and third columns; that is, the conditional precipitation and PDF of CWV are insensitive to spatial resolution, with small but noticeable decreases in the PDF at highest CWV (above critical). This insensitivity is consistent with the assertion that the autocorrelation spatial scales of CWV and tropospheric temperature are much greater than that of precipitation. Nonetheless, to what extent this holds depends on the gap filling (Figs. S9–S11 in section S4). It is also consistent with Yano et al. (2012), which used a cloud-resolving model (CRM) and demonstrated that the conditional precipitation as a function of CWV is quantitatively robust to spatial resolution (up to ~1°).

The conditional probability defined by a fixed nonzero threshold (1.05 mm h^{-1}; Fig. 1, second column) slightly shifts toward lower CWV with spatial coarse graining, consistent with the greater chances of observing precipitation over a

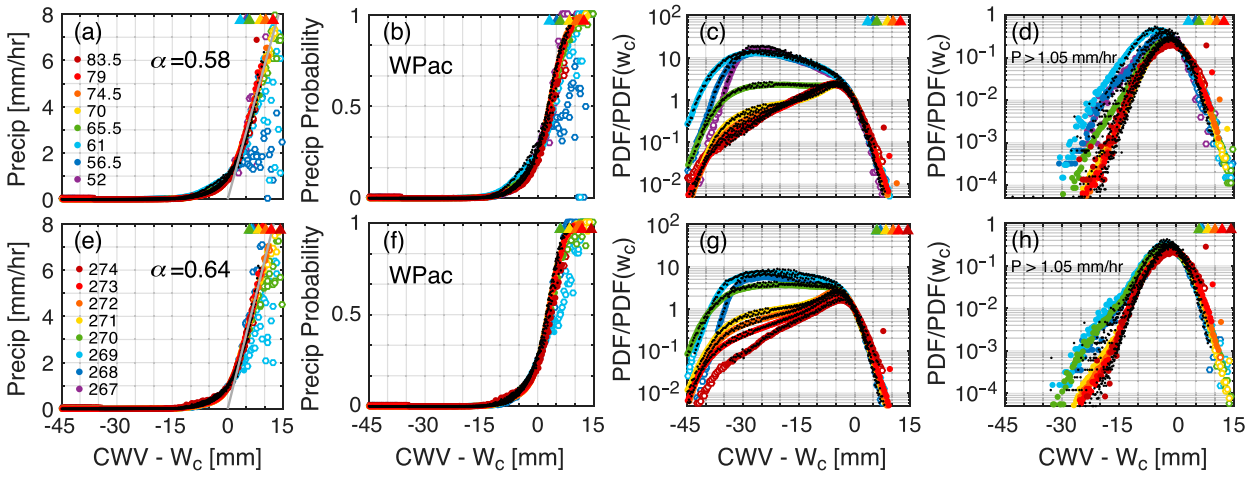

FIG. 2. (a)–(d) Convective transition statistics for the tropical western Pacific as in Figs. 1a–d for 0.25° (colored markers) and 0.5° (dots), but for each marker/dot shifted by the corresponding critical CWV (w_c) from Fig. 3c, and with PDFs scaled. The best fit for conditional precipitation is shown as a gray line in (a), with its slope indicated by α. (e)–(h) As in (a)–(d), but using $\hat{T}$ instead of $\widehat{q_{sat}}$ as the bulk tropospheric temperature measure. The colored triangles represent average $\widehat{q_{sat}}$ conditioned on $\hat{T}$ and CRH ($\equiv$CWV/$\widehat{q_{sat}}$) > 60%, shifted by w_c. The corresponding plots for the other basins are in Figs. S5 and S6.

larger area. However, with a much higher threshold (e.g., 15 mm h^{-1}, the practical maximum for TMIv7.1 precipitation in the tropics) or at even lower resolution (e.g., 2°), the dependence on spatial resolution may reverse for the rarer chances of seeing extreme rainfall over a larger area. These dependences indicate the underlying joint PDF of CWV and P being resolution sensitive, as will be discussed in section 6.

b. Critical CWV and collapsed statistics

As described earlier, CWV measures the impact of environment moisture on conditional instability, and hence precipitation. For those $\widehat{q_{sat}}$ bins most relevant in the tropics (≥61 mm), the pickup curves in Fig. 1 suggest the possibility of collapsing statistics by shifting CWV by w_c for each $\widehat{q_{sat}}$, that is, the precipitation–CWV relation can be simplified by taking into account the dependence of w_c on temperature. To define w_c as a function of $\widehat{q_{sat}}$, it makes sense to do so based on conditional precipitation alone, for it, unlike the conditional probability, does not rely on any threshold and is insensitive to spatial resolution. This assumes that the conditional precipitation has the form of f(CWV − w_c), with its $\widehat{q_{sat}}$ dependence implicitly built in through $w_c(\widehat{q_{sat}})$. See section S3 regarding details on finding w_c given the statistics as in Fig. 1.

Figures 2a–d show the collapsed version of the original statistics for the tropical western Pacific in Figs. 1a–d (other basins in Fig. S6). As in Fig. 2a, w_c is defined as the CWV value at which the best fit for conditional precipitation (gray line) intersects with the CWV axis. For $\widehat{q_{sat}}$ bins ≥70 mm, the conditional precipitation, probability of precipitation (Fig. 2b), and PDF of precipitating events (Fig. 2d) collapse perfectly. For these $\widehat{q_{sat}}$ bins, there are below-critical precipitating events, many of which are weakly precipitating and excluded because of the 1.05 mm h^{-1} threshold adopted here, and are likely associated with the mature and decaying phases of convection (not shown). As $\widehat{q_{sat}}$ increases, $\widehat{q_{sat}} - w_c$ (triangles) increases, indicating critical deviates from column saturation. For lower $\widehat{q_{sat}} \leq 61$ mm, both conditional precipitation and probability have slightly higher (lower) values for CWV right below (above) critical, with some underpopulated CWV bins (open circles) exceeding the corresponding column saturation (triangles), indicating minor inconsistency between the retrieval and reanalysis datasets. Furthermore, there is more below-critical precipitation as $\widehat{q_{sat}}$ decreases (Fig. 2d; even more when a smaller precipitation threshold is adopted), consistent with cold events originating from the extratropics and exhibiting characteristics different from deep convection in the tropics.

The PDF of CWV in Fig. 2c also collapses around and above critical, with the PDF of nonprecipitating events (including those with $P < 1.05$ mm h^{-1}) varying with $\widehat{q_{sat}}$ and basin. For CWV slightly lower than critical, the PDF of CWV starts to drop rapidly, and the PDF for precipitating events peaks. As demonstrated in simple stochastic models (Stechmann and Neelin 2011, 2014), moisture accumulates by surface evaporation and moisture convergence until CWV reaches critical, at which point precipitation becomes an effective sink, leading to the drop in the PDF for CWV above critical. Note that the PDF for all events has another peak at lower CWV because of the balance between surface evaporation and moisture divergence.

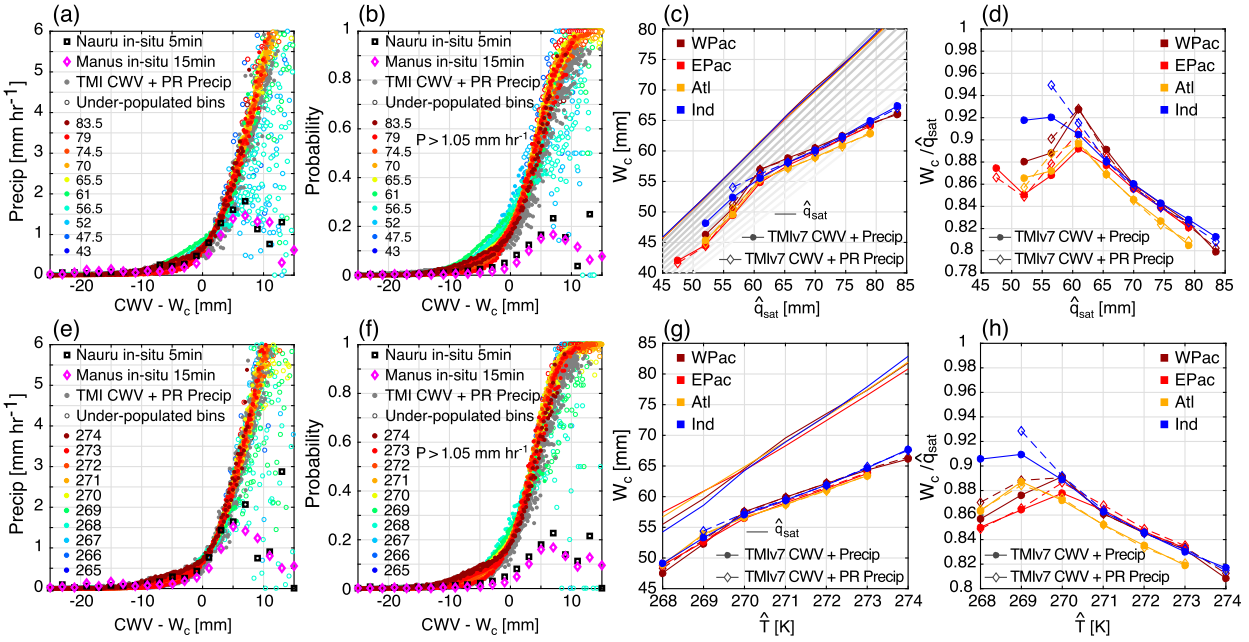

FIG. 3. (a) Collapsed conditional precipitation, (b) probability of precipitation, and (c) critical CWV w_c and (d) critical CRH ($\equiv w_c/\widehat{q_{\rm sat}}$) for tropical oceans using $\widehat{q_{\rm sat}}$ as the bulk tropospheric temperature measure. (e)–(h) As in (a)–(d), but using $\hat{T}$ instead of $\widehat{q_{\rm sat}}$ as the bulk temperature. The conditional precipitation [(a), (e)] and probability of precipitation [(b), (f); $P > 1.05\,{\rm mm\,h^{-1}}$] are compiled for three combinations of datasets: (i) TMIv7.1 CWV and precipitation (colored dots) with underpopulated bins plotted as open circles, (ii) TMIv7.1 CWV and PR 2A25 precipitation (gray dots) excluding underpopulated bins, and (iii) ARM site CWV and precipitation measurements from Manus (diamonds) and Nauru (squares) Islands in the tropical western Pacific (WPac). Reanalysis-2 temperature is used for (i)–(iii). For (i) and (ii), bins from all four basins are plotted, with data at 0.25° resolution and coastal regions excluded. For (iii), the CWV values are shifted by the corresponding w_c given the temperature ($\widehat{q_{\rm sat}}$ or $\hat{T}$) time series according the w_c–temperature relation for WPac [as in (c) and (g)]. The critical CWV [(c), (g)] and critical CRH [(d), (h)] are calculated for combinations (i) and (ii), respectively. The colored solid lines in (c) and (g) represent $\widehat{q_{\rm sat}}$ conditioned on temperature and CRH ($\equiv$CWV/$\widehat{q_{\rm sat}}$) > 60%. This conditional $\widehat{q_{\rm sat}}$ is also used in defining the critical CRH. The gray lines in (c) represent CRH from 100% to 80% with 2% spacing.

Earlier studies (Neelin et al. 2009; Sahany et al. 2014) have suggested scaling instead of shifting by w_c, that is, considering the form $f({\rm CWV}/w_c)$ instead of the shift $f({\rm CWV} - w_c)$, to collapse the statistics. Both are similar to leading order for small differences in w_c, but to second order have slightly different effects. Scaling preserves the zero CWV value, which can be important when examining PDFs across the entire CWV range, while shifting is preferred here because effects near critical seem to be affected by factors that do not scale with w_c. The two approaches may lead to different interpretations for warming climate, where some of the simplest arguments tend to rescale moisture by saturation [see Camargo et al. (2014) for a discussion surrounding saturation deficit versus relative humidity in projecting future tropical cyclone genesis frequency].

c. *Dependence of critical on temperature*

The collapsed conditional precipitation and probability of precipitation for the tropical western Pacific at 0.25° in Figs. 2a and 2b are duplicated in Figs. 3a and 3b, along with the critical CWV $w_c(\widehat{q_{\rm sat}})$ (Fig. 3c) and critical CRH $w_c(\widehat{q_{\rm sat}})/\widehat{q_{\rm sat}}$ (Fig. 3d). Results for other basins are also shown. Here, we focus on the results derived using TMIv7.1 CWV and precipitation.

In Figs. 3a–d, the precipitation pickup and the dependence of w_c on $\widehat{q_{\rm sat}}$ are constant across basins, with slightly lower w_c for the tropical Atlantic. As noted earlier, a clear transition occurs around $\widehat{q_{\rm sat}} = 61$ mm in Figs. 3c and 3d. For lower $\widehat{q_{\rm sat}}$, the precipitation pickup is less well defined and scatters more, and so do the corresponding critical values, with approximately constant critical CRH. Above the transition $\widehat{q_{\rm sat}}$, the critical values deviate from saturation as $\widehat{q_{\rm sat}}$ increases, that is, deep convective onset occurs at higher CWV but at lower CRH with increasing tropospheric temperature, as shown in Neelin et al. (2009). The critical CRH decreasing with $\widehat{q_{\rm sat}}$ is expected to be robust as long as w_c is defined through collapsing statistics, for other reasonable definitions of critical [e.g., assuming the functional form of $\log[1 + e^{\alpha({\rm CWV}-w_c)}]$ for the conditional precipitation] would only introduce a $\widehat{q_{\rm sat}}$-independent

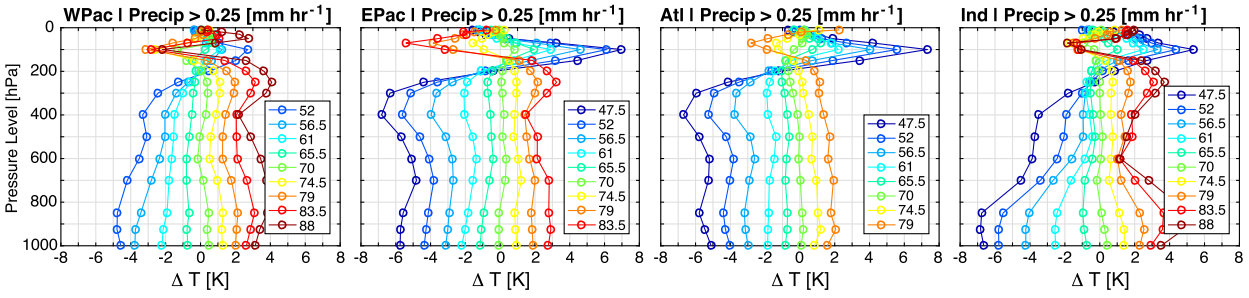

FIG. 4. Reanalysis-2 temperature profiles conditionally averaged on TMIv7.1 precipitation and $\widehat{q_{\rm sat}}$. Profiles are anomalies with respect to the mean profile averaged over all precipitating events ($P > 0.25$ mm h^{-1}) with coastal regions excluded.

offset of w_c, preserving the slope of the w_c–$\widehat{q_{\rm sat}}$ relation that, when compared with the constant CRH (gray) lines in Fig. 3c, indicates decreasing critical CRH with $\widehat{q_{\rm sat}}$.

The transition from approximately constant to decreasing critical CRH with increasing $\widehat{q_{\rm sat}}$ marks the different precipitation regimes, that is, convection dominant in the tropics versus large-scale saturation driven in the extratropics.

d. Robustness to instrumentation

Before the convective transition statistics can be used for model diagnostics, their robustness and sensitivity to instrumentation must be quantified. Figures 3a–d include the results derived using multiple datasets, including (i) TMIv7.1 CWV and precipitation, (ii) TMIv7.1 CWV and PR 2A25 precipitation, and (iii) ground-based measurements from Manus and Nauru ARM sites in the tropical western Pacific.

The statistics in Figs. 3a–d are robust to TMIv7.1 versus PR precipitation, with slightly more scatter for the conditional probability. Combining TMIv7.1 CWV and 3B42 precipitation results in quantitatively similar statistics except for a slightly smaller slope α of the best fit for conditional precipitation (not shown).

In Fig. 3a, the conditional precipitation from Manus and Nauru ground-based measurements, collapsed using $w_c(\widehat{q_{\rm sat}})$ for the tropical western Pacific (WPac; TMIv7.1 CWV + precipitation), are quantitatively consistent with those from satellite retrievals, with significant low bias at highest CWV (relative to critical; CWV $- w_c > 5$ mm); the corresponding conditional probability in Fig. 3b is uniformly lower than satellite retrievals because of the difference in spatial resolution, with the similar low bias. Combining the ground-based CWV time series and 3B42 precipitation around Manus and Nauru shows the same bias at high CWV, indicating that the cause is due to the ground-based MWR CWV measurements (section S8). These have a wet-window problem, that is, high CWV events associated with strong precipitation are missing in the raw CWV time series, and gap filling can only partially compensate for this.

Although not the focus here, conditional precipitation and probability at the Manaus GOAmazon site (over land) exhibits quantitative differences from those over oceans as in Fig. 3, despite the qualitative similarities we shall discuss in section 5.

The quantitative agreement among datasets examined here boosts our confidence in the reliability of the convective transition statistics as model diagnostic tools. Meanwhile, given that the same TMIv7.1 CWV and Reanalysis-2 temperature are used for compiling the statistics, we advise caution that the robustness of the statistics to TMIv7.1 versus PR precipitation may simply reflect the efforts of calibration among datasets. As indicated by the minor difference in the collapsed conditional probabilities in Fig. 3b, and as we shall see in section 6, the two precipitation datasets do lead to quantitative differences in the distribution of precipitation, especially at high rain rate.

e. Robustness to bulk measure of temperature

Thus far, $\widehat{q_{\rm sat}}$ appears to be a useful bulk measure of tropospheric temperature. As noted above, the critical value is not governed by $\widehat{q_{\rm sat}}$ in a simple way, with critical CWV increasing and critical CRH decreasing with $\widehat{q_{\rm sat}}$.

Figure 4 shows the temperature profile, conditioned on precipitation and $\widehat{q_{\rm sat}}$, relative to the mean profile (referred to as a perturbation). The perturbed profile evolves coherently in the vertical as a function of $\widehat{q_{\rm sat}}$, explaining the usefulness of a bulk temperature measure such as $\widehat{q_{\rm sat}}$, or the mass-weighted column-averaged temperature $\hat{T}$ adopted in previous studies (e.g., Holloway and Neelin 2007; Sahany et al. 2012). The profiles are similar across basins, except for the high- and low-$\widehat{q_{\rm sat}}$ bins in the tropical Indian Ocean showing greater (smaller) anomaly in the lower (upper) troposphere. This is likely a consequence of the circulation pattern driven by the local land–ocean contrast, since both the warmest and coldest events in this domain tend

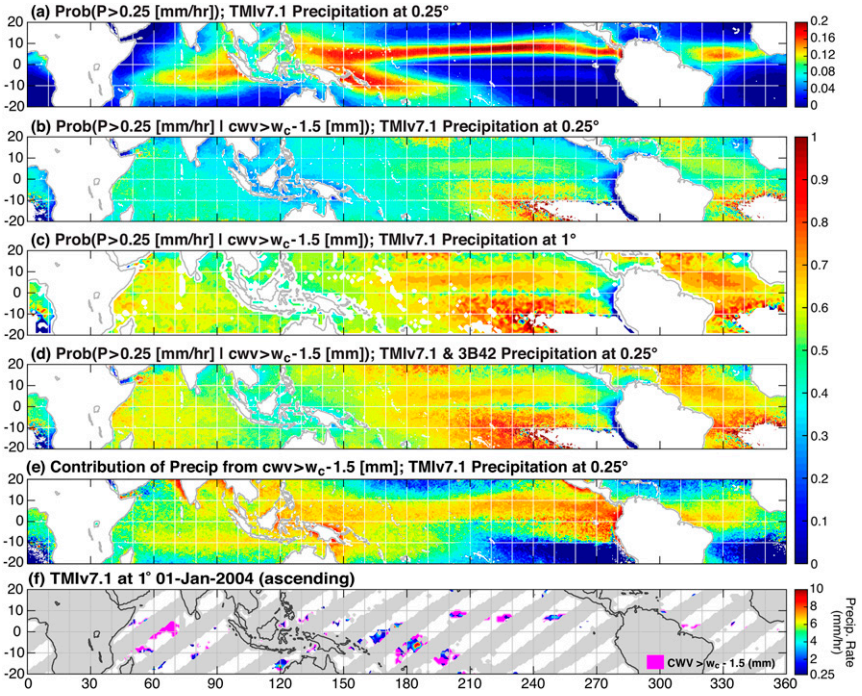

FIG. 5. (a) The probability of precipitation as a function of geographical location, calculated using TMIv7.1 precipitation at 0.25° resolution. (b) The conditional probability of precipitation given CWV exceeding critical, calculated using TMIv7.1 CWV and precipitation, and Reanalysis-2 temperature at 0.25°. Here the conditional probability is calculated from the frequency binned by CWV $- w_c(\widehat{q_{\rm sat}})$, P, and geographical location, with $w_c(\widehat{q_{\rm sat}})$ as in Fig. 3c averaged over four basins. (c) As in (b), but at 1°. (d) As in (b), but with P defined as the maximum of the TMIv7.1 precipitation rate and two additional 3B42 precipitation rates that are closest in time to the TMIv7.1 measurement. (e) The fraction of total precipitation from events with CWV exceeding critical, calculated using data as in (b) at 0.25°. (f) Precipitation rate (for $P \geq 0.25\ {\rm mm\ h^{-1}}$) on top of regions of CWV exceeding critical using TMIv7.1 data at 1° for ascending orbits on 1 Jan 2004. Note that (f) is a realization of the conditional probability in (c) on a particular day. For (a)–(e), the precipitation threshold $0.25\ {\rm mm\ h^{-1}}$ is chosen for comparison across spatial resolution, and CWV offset -1.5 mm to include more events. The magnitudes of probabilities/fraction in these panels depend on the precipitation threshold and CWV offset, while the corresponding geographic patterns appear to be robust.

to occur near the South Asian continent in the Bay of Bengal and Arabian Sea (Fig. S13). The resulting statistics in Figs. 1–3, nevertheless, do not reflect this difference in temperature structure. Replacing the condition on precipitation by CWV above critical, or replacing $\widehat{q_{\rm sat}}$ by $\hat{T}$, leads to similar profiles. For $\widehat{q_{\rm sat}}$ higher than the most probable bin, the corresponding overall (perturbed + mean) temperature profiles are insensitive to conditions on precipitation or CWV, suggesting that high-$\widehat{q_{\rm sat}}$ events result from previous or nearby convective activity, consistent with convection being the major heating mechanism in the tropical troposphere.

The two bulk measures $\widehat{q_{\rm sat}}$ and $\hat{T}$, both of which have similar properties in characterizing convection, are well correlated because of the vertical coherence of temperature (section S2). It is nonetheless worth quantifying in detail their similarity as bulk temperature measures for the statistics because of the nonlinear dependence of precipitation statistics on the thermodynamic variables. The bottom panels of Figs. 2 and 3 show the similar statistics corresponding to their top-panel counterparts, but use $\hat{T}$ instead as the bulk measure (other basins in Fig. S5). From these two figures, substituting one bulk measure by another only leads to minor quantitative differences, for example, a slightly smaller slope α for conditional precipitation (Fig. 2a vs Fig. 2e), and slightly more precipitating events for CWV right below critical for cold bins when $\widehat{q_{\rm sat}}$ is used (Fig. 2d vs Fig. 2h). This insensitivity to the bulk measure of temperature also holds for statistics presented in Figs. 5 and 7–9 below. Note that the vertically coherent temperature structure in the presence of convection

guarantees that layered bulk measures (e.g., 850–500-hPa integrated saturation humidity) can also be useful and would lead to similar statistics (e.g., Figs. 1 and 3 in Neelin et al. 2009), except for the PDF of all events for CWV significantly lower than critical, which could differ qualitatively (not shown).

4. Geographical dependence of precipitation pickup

The statistics in Figs. 2 and 3 demonstrate that CWV above critical is a practical estimator of conditional instability, and hence precipitation, with the temperature dependence characterized by the w_c–temperature relation [$w_c(\widehat{q_{\rm sat}})$ or $w_c(\hat{T})$]. These relations seem to be universal across ocean basins, at basin scales. However, other factors contributing to conditional instability—vertical degrees of freedom of temperature and moisture structure not captured by the bulk measures used here, large-scale convergence/divergence, radiative forcing associated with existing clouds or the lack thereof, and triggering of convection because of cold pool expansion from organized systems or land–sea breeze in coastal regions—may vary geographically, causing geographic variations at regional scales (e.g., Torri et al. 2015; Bergemann and Jakob 2016; Ahmed and Schumacher 2017). As such, the effectiveness of CWV above critical as a predictor of precipitation at regional scales is examined in this section.

As background for our discussion, Fig. 5a shows the probability of precipitation ($P > 0.25\,\mathrm{mm\,h^{-1}}$; details in caption). The probability of high CWV (relative to critical; Fig. S14a) is included in section S7. These maps of probability of precipitation and high CWV reflect the climatology of precipitation (Fig. S14b), sharply contrasting the major convergence zones with regions elsewhere.

Figure 5b shows the corresponding conditional probability of precipitation given high CWV, formally defined as

$$\mathrm{Prob}(P > 0.25\,\mathrm{mm\,h^{-1}} | \mathrm{CWV} > w_c - 1.5\,\mathrm{mm}) \equiv \frac{\text{No. of occurences with } P > 0.25\,\mathrm{mm\,h^{-1}} \text{ and } \mathrm{CWV} > w_c - 1.5\,\mathrm{mm}}{\text{No. of occurences with } \mathrm{CWV} > w_c - 1.5\,\mathrm{mm}},$$

as a function of geographical location. Here the critical value $w_c(\widehat{q_{\rm sat}})$ is from Fig. 3c, averaged over four basins (adopting basin-dependent critical values only introduces small discontinuities in w_c, hence the conditional probability across basin boundaries). The most outstanding feature in Fig. 5b is that the conditional probability is far smoother than the probability of precipitation in Fig. 5a. To the extent that there are geographic variations, the conditional probability scarcely reflects the features of precipitation climatology. Thus, including CWV relative to critical and the dependence of critical on temperature has yielded a probability measure that is much less dependent on space.

To a first approximation, the CWV value relative to critical thus provides information that will apply reasonably well across a large portion of the tropics. Furthermore, compiling the statistics presented in Fig. 3 inside and outside regions with high seasonal precipitation yields quantitatively similar results (not shown; refer to Fig. 3 since the corresponding collapsed statistics and critical values are visually indistinguishable), reaffirming that these statistics focus on the occurrences of convection at fast time scales rather than long-term climatology.

Minor geographic variations may be noted in Fig. 5b, for example, the contrast between the lower values around the Maritime Continent and along the equator in the eastern Pacific, and the higher values off the equator in the central to eastern Pacific and Atlantic. The conditional probability is not defined over dry regions covered by marine stratocumulus (there are not above-critical events occurring in these locations); where it is defined, there is large uncertainty associated with small sample size along the edges of the dry regions (e.g., along 10°S in the eastern Pacific). The extreme low values in some coastal regions (~2.5° in width, the resolution of Reanalysis-2 data) could be due to physical coastal effects (Bergemann and Jakob 2016). However, local decreases in the temperature (Fig. 3 in Kuo et al. 2017) suggest they are more likely due to the erroneously lower $\widehat{q_{\rm sat}}$ (and hence w_c) and spurious occurrence of above-critical events arising from land–ocean temperature contrasts and spatial interpolation.

Figures 5c and 5d further quantify spatial and temporal dependence of this conditional probability. Figure 5c shows the same conditional probability as in Fig. 5b, but at 1°. Coarse graining in space leads to the same spatial pattern (or the lack thereof) and, with the $0.25\,\mathrm{mm\,h^{-1}}$ threshold adopted here, uniformly greater magnitude in conditional probability, consistent with the dependence on resolution shown in Figs. 1 and 2. That is, CWV above critical serves as a precipitation estimator with more certainty at scales comparable to or larger than the autocorrelation spatial scale of precipitation.

Figure 5d shows the conditional probability as in Fig. 5b, but incorporating 3B42 precipitation (details in caption). Here, including two additional 3B42 precipitation rate values effectively provides one more independent snapshot of precipitation taken in the period of 0–4.5 h prior to or after the TMIv7.1 measurement is acquired. The resulting conditional probability in Fig. 5d therefore quantifies the probability of observing at least one precipitating event from the two datasets, consecutive in time but randomly separated by up to 4.5 h, given that CWV exceeds critical. Note that here the CWV value relative to critical is treated as approximately constant because of the long autocorrelation time scales of CWV and temperature.

As expected, the conditional probability in Fig. 5d (at 0.25°) is everywhere greater than its counterpart in Fig. 5b, and a similar map compiled at 2° is uniformly greater than 85% over tropical oceans (not shown). These suggest that, at scales comparable to the autocorrelation spatial and temporal scales of CWV, an above-critical event is almost certainly accompanied by precipitation before decreasing to below critical. While precipitation has much shorter autocorrelation time scales, the comparison of Figs. 5b and 5d has ruled out the simplest hypothesis that the two consecutive-in-time measurements of precipitation can be treated as independent random events (not shown).

Figure 5e shows the fraction of total precipitation from above-critical events, which are responsible for most of the precipitation over tropical oceans (except in dry regions). It also captures the seasonal shifts of convergence zones, for example, the local maximum along 10°S in the Indian Ocean and between 0° and 10°S in the eastern Pacific results from events during the Southern Hemisphere raining seasons.

Note that Fig. 5e [and the conditional probability $\mathrm{Prob}(\mathrm{CWV} > w_c - 1.5\,\mathrm{mm} \mid P > 0.25\,\mathrm{mm\,h^{-1}})$; Fig. S14d] has a geographic pattern similar to Fig. 17 in Tao and Moncrieff (2009; fraction of precipitation from mesoscale convective systems) with some coastal exceptions. This similarity suggests that organized systems are important contributors to precipitation above critical (see also Moncrieff et al. 2017). As we have seen in Figs. 1 and 2, the conditional precipitation and PDF of CWV are robust to spatial resolution (up to ~1°); in addition to the autocorrelation spatial scale of CWV being greater than that of precipitation, organized systems could play a role in this robustness.

Finally, Fig. 5f shows an example for ascending orbits on a particular day, showing the regions where CWV is close to or above critical, that is, a realization of the conditional probability in Fig. 5c for those snapshots on each orbit. Precipitation values exceeding $0.25\,\mathrm{mm\,h^{-1}}$ are overlaid. It may be seen that precipitation mainly occurs in the near- or above-critical regions sporadically, consistent with the probabilities shown in the earlier panels. Thus, the estimates of near- or above-critical CWV–temperature environment may have useful applications as predictors of precipitation (see also section S7), making the known association of precipitation with high CWV (e.g., Mapes et al. 2006) more quantitative.

5. Sensitivity to time averaging

Satellite retrievals provide snapshots of CWV and precipitation covering basin-scale areas and, unlike most ground-based data, contain enough events for the compiled statistics to be stable, that is, insensitive to noise. However, when these statistics apply to model diagnostics—given that most current models output at subdaily frequencies (e.g., 6- or 12-hourly means) and higher-frequency output (e.g., hourly or time-step mean/snapshot) are not standard yet—the validity of the model versus retrieval comparison must be addressed. To quantify the dependence on coarse graining in time, we turn to ground-based measurements that have more extensive time-domain information.

Figure 6 shows statistics from tropical ARM site measurements with different time averaging (not conditioned on temperature). At these sites, the temperature range in terms of $\hat{T}$ is narrow, with ~1–2-K variation, and hence the overall statistics are dominated by the most probable temperature bin. The conditional precipitation (first column) and frequency density for all events (third column, crosses) are relatively insensitive to time averaging up to 6 h, with Nauru being more sensitive than the other two sites. Conditional probability (second column; $P > 0.5\,\mathrm{mm\,h^{-1}}$) increases with time averaging, reflecting the sensitivity of the joint PDF of CWV and precipitation. There are quantitative differences among these sites, but there is not a clear qualitative difference or contrast between oceanic versus continental environments regarding the dependence on time averaging. The sharpness of the pickup tends to be smoothed out by the averaging, resulting from averaging subdaily instances of high CWV, high precipitation times with lower values. Overall, however, the results in Fig. 6 suggest that, while instantaneous or hourly data are desirable for insights into the fast-time-scale behavior, statistics from 3- or 6-hourly mean data can be used for model comparisons, extending the applicability of using these statistics as diagnostic tools.

6. Joint PDF of CWV and precipitation, and its resolution/instrument dependence

As mentioned in section 4, bulk measures like CWV and $\widehat{q_{\mathrm{sat}}}$ (or $\hat{T}$) can represent large-scale factors that

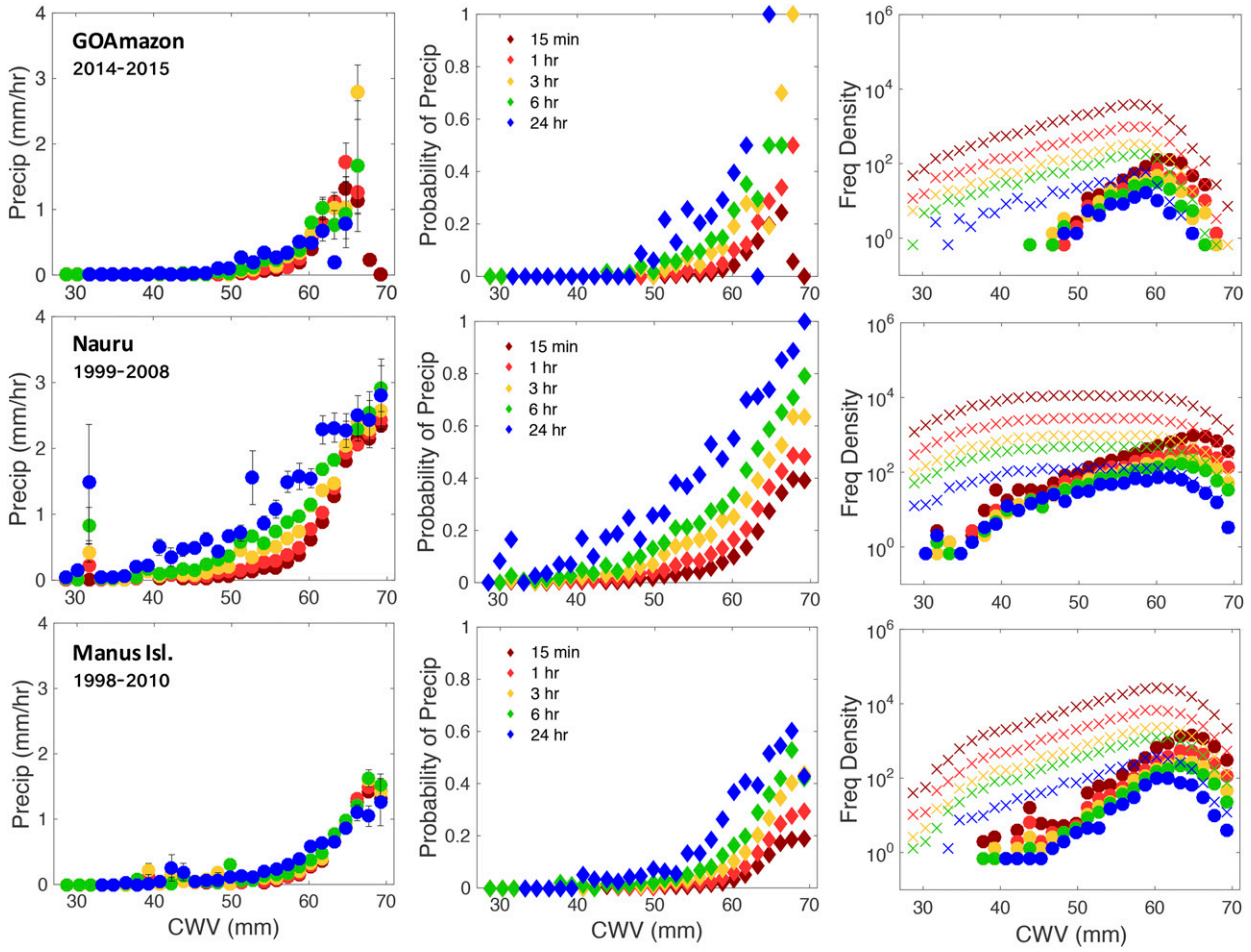

FIG. 6. (left) Precipitation rate with standard error as an error bar, (center) probability of precipitation $P > 0.5\,\mathrm{mm\,h^{-1}}$, and (right) frequency density of all events (crosses) and precipitating events (circles), all conditioned on CWV using ARM site microwave radiometer CWV and precipitation data for (top) the GOAmazon site in the Amazon and for (middle) Nauru and (bottom) Manus Islands in the tropical western Pacific. Here the statistics are calculated using CWV and precipitation data time averaged at 15-min (dark red), 1-h (red), 3-h (yellow), 6-h (green), and 24-h (blue) intervals. Conditional precipitation without an error bar indicates a standard error smaller than the marker size.

affect conditional instability. However, given the same condition at large scales, one would still expect a distribution of precipitation because there are processes at smaller scales or large-scale factors that are unaccounted for by the bulk measures. In this section, we examine the joint PDF of CWV and precipitation, and its dependence on spatial resolution and instrumentation, to quantify the uncertainty associated with the use of the bulk measures. This joint PDF can be another useful metric for model diagnostics.

Figure 7a shows the joint PDF of CWV (relative to critical) and precipitation rate P for the 70-mm $\widehat{q_{\mathrm{sat}}}$ bin (second-most probable) in the tropical western Pacific compiled using PR (2A25) precipitation at 0.25°. This $\widehat{q_{\mathrm{sat}}}$ bin is chosen instead of the most probable bin (74.5 mm) because for the latter, the 75-mm cap of TMIv7.1 CWV results in the CWV value relative to critical being capped at ~11 mm, and hence the PDF of the highest CWV is missing. The same joint PDF is plotted in Fig. 7b on a log–log scale. Nonprecipitating bins ($0 \le P < 0.05\,\mathrm{mm\,h^{-1}}$) aside, the joint PDF is quantitatively similar across the $\widehat{q_{\mathrm{sat}}}$ range and ocean basins (section S5).

For CWV below critical, the PDF in Fig. 7a drops sharply as P increases. As the CWV increases and approaches critical, the PDF increases for all $P > 0$ with long tails extending into high precipitation regime. This occurs until the CWV reaches critical, above which the PDF starts to decrease, with a local PDF maximum developing at a positive P (~$3\,\mathrm{mm\,h^{-1}}$) for the highest CWV bin. From Figs. 7a and 7b (the same joint PDF on different scales), there is not a clear power law or

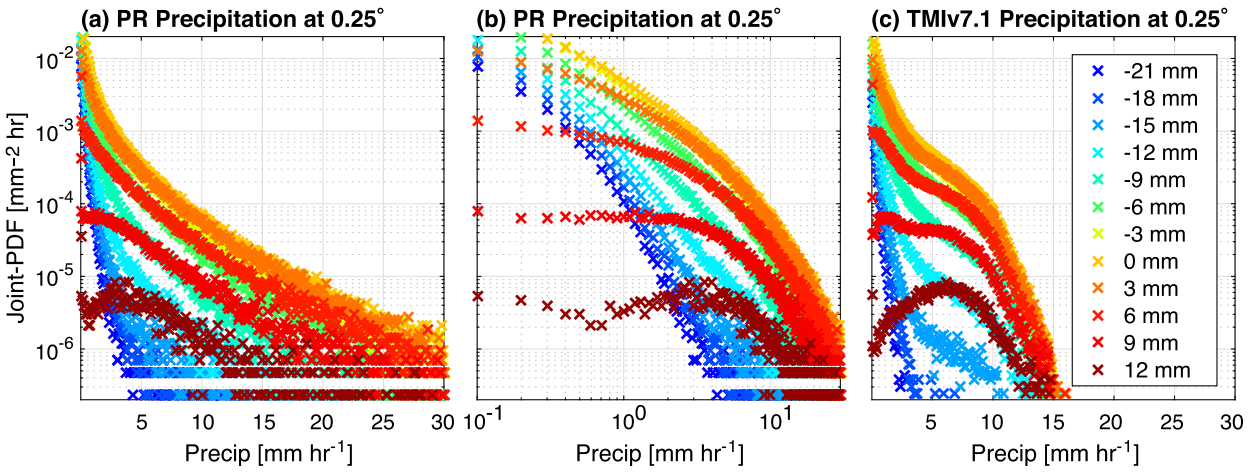

FIG. 7. (a) Joint PDF of CWV relative to critical and precipitation rate P for the 70-mm $\widehat{q_{\text{sat}}}$ bin in the tropical western Pacific compiled using TMIv7.1 CWV, Reanalysis-2 temperature, and PR 2A25 precipitation at 0.25° by treating CWV and P as continuous variables with bin width 3 mm, and 0.1 mm h^{-1} (0.05 mm h^{-1} for lowest bin), respectively. (b) As in (a), but on a log–log scale. (c) As in (a), but using TMIv7.1 precipitation (0.25°). The colors indicate the values of CWV relative to w_c.

exponential dependence of the PDF on precipitation, although a possible functional form will be discussed further below.

Note that the distribution of P is asymmetric, with the most probable value being (close to) zero even for CWV around critical. As such, any Gaussian-like distribution (Lin and Neelin 2003) or on-and-off precipitation model (Muller et al. 2009; Stechmann and Neelin 2014) with the observed conditional mean and variance would miss much of the distribution details.

The radar-based precipitation retrievals are probably more reliable than the passive microwave radiometer counterpart (including TMI) since the latter is based solely on a path-integrated signal without phase information (Chen et al. 2013). The conditional precipitation and probability of precipitation in Fig. 3 demonstrate that PR 2A25 and TMIv7.1 precipitation are consistent in terms of the mean and distribution of low to moderate precipitation. However, there are quantitative discrepancies for high precipitation between the two datasets. Figure 7c shows the similar joint PDF as in Fig. 7a, but using TMIv7.1 precipitation instead. In Fig. 7c, there is a clear cutoff at $P \sim 10\,\text{mm}\,\text{h}^{-1}$ and practically no events for >15, despite that the cap set by the algorithm is 25. This is an undesirable characteristic of the retrieval algorithm when applied to the tropics (there is no sign of a cutoff in the extratropics; not shown). Besides the cutoff, the joint PDFs for $P < 10\,\text{mm}\,\text{h}^{-1}$ are similar for PR and TMIv7.1, with minor quantitative differences, for example, the local PDF maximum at high CWV occurs at higher precipitation for TMIv7.1. Thus, we shall not emphasize the distribution of precipitation from TMIv7.1 precipitation, except for using it as an aid to study its dependence on spatial resolution.

Figure 8 shows the joint PDF of CWV (relative to critical) and P compiled at different spatial resolutions (details in caption). The two panels for 0.25° show the same joint PDFs as in Figs. 7a and 7c, but with a different CWV bin width.

In terms of the general features, the joint PDFs in Fig. 8 exhibit clear asymmetries between the low CWV–low precipitation regime and regime near critical. However, in the vicinity of critical (roughly ±3 mm), the joint PDFs are roughly symmetric with respect to CWV, consistent with Figs. 2d and 2h. As CWV increases, the fraction of nonprecipitating events decreases, as indicated by the conditional probability of precipitation (orange dots; $P > 0$) and the bands at the bottom for the top three panels (PDFs for $0 \le P < 0.05\,\text{mm}\,\text{h}^{-1}$). This and the extension of PDF into high precipitation around critical result in the sharp increase in the conditional mean (blue solid line), median (white solid), and variance (blue dashed) of precipitation. These three conditional statistics, when calculated by excluding nonprecipitating pixels, would still show a sharp pickup around critical with slightly higher values for CWV below (not shown). Both the precipitation distribution for $P > 0$ and its contrast to nonprecipitating events (i.e., $P > 0$ versus $P = 0$) contribute to the overall variance of precipitation (Stechmann and Neelin 2011).

In addition to the differences of PR and TMIv7.1 shown in Fig. 7, the conditional probability for PR at 0.25° in Fig. 8 is noticeably higher than its TMIv7.1 counterpart for CWV lower than critical, partly because of the differences in instrument sensitivity and native

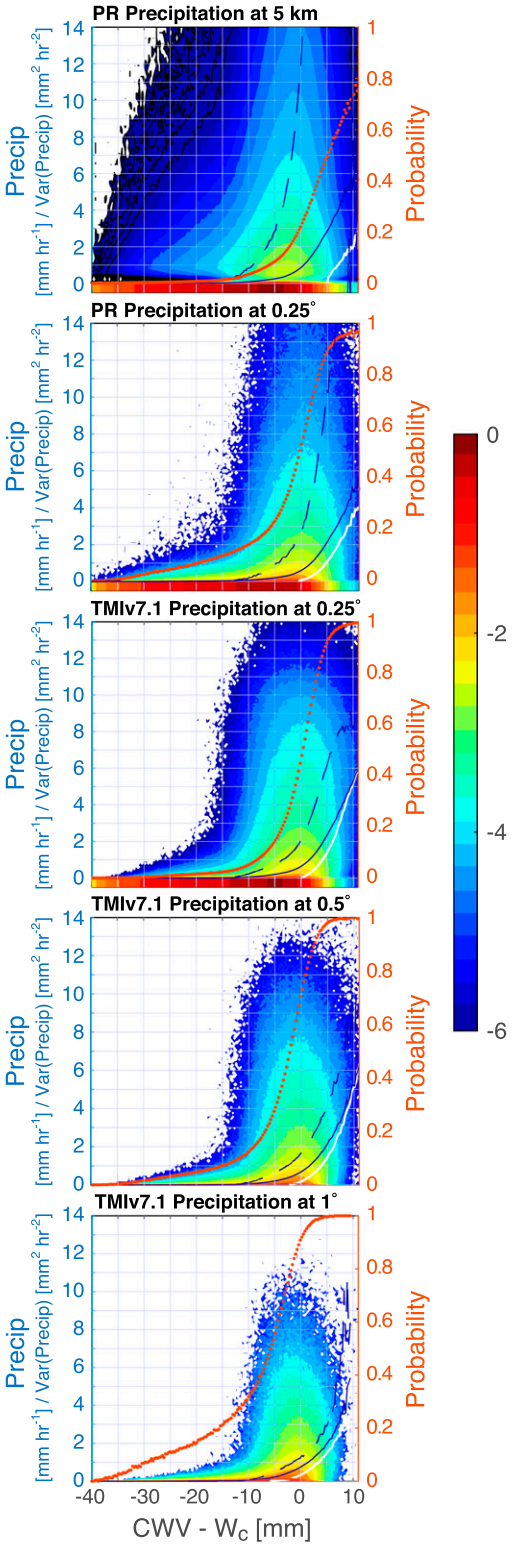

FIG. 8. Joint PDF (color shading; $\mathrm{mm}^{-2}\,\mathrm{h}$), on a $\log_{10}$ scale, of CWV relative to critical and precipitation rate P for the 70-mm $\widehat{q_{\mathrm{sat}}}$ bin in the tropical western Pacific compiled using TMIv7.1 CWV and Reanalysis-2 temperature, PR 2A25 (at 5 km and 0.25°) and TMIv7.1 (at 0.25°, 0.5°, and 1°) precipitation, by treating CWV and P as continuous variables. The spacing between the joint PDF contours is 0.3, that is, the color advances whenever the joint PDF doubles ($10^{0.3} \sim 2$). The corresponding precipitation rate (solid blue line), probability of precipitation ($P > 0\,\mathrm{mm\,h^{-1}}$; orange dots), median (solid white line), and variance (dashed blue line) of precipitation, all conditioned on CWV, are also shown for reference. For PR (at 5 km and 0.25°) and TMIv7.1 (0.25°), the bands at the bottom indicate bins with $0 \le P < 0.05\,\mathrm{mm\,h^{-1}}$. Note that the minimum nonzero P for raw PR data at 5 km is $\sim 0.11\,\mathrm{mm\,h^{-1}}$, and the TMIv7.1 precipitation at 0.25° is discretized with units $0.1\,\mathrm{mm\,h^{-1}}$.

resolution of the datasets. Recall in Fig. 3 that the conditional mean and probability (with respect to a different $1.05\,\mathrm{mm\,h^{-1}}$ threshold) from PR and TMIv7.1 are extremely close. Despite this, the two 0.25° panels in Fig. 8 show that the TMIv7.1 precipitation tends to underestimate the variance of precipitation for CWV around and above critical. Furthermore, the TMIv7.1 conditional median approaches mean at high CWV, implying a more symmetric distribution of precipitation, consistent with the corresponding PDFs in Fig. 7c.

As for the dependence on spatial resolution shown in Fig. 8, there are more weakly precipitating events (e.g., $0 < P < 2\,\mathrm{mm\,h^{-1}}$) in the expense of nonprecipitating and heavily precipitating events at lower resolutions, consistent with spatial averaging, which also results in the conditional probability increasing and variance decreasing with resolution.

Figure 9 shows the precipitation contribution as a function of CWV and P for the 70-mm $\widehat{q_{\mathrm{sat}}}$ bin in the tropical western Pacific on different scales. In Fig. 9a, the areas under the curve integrated to the mean precipitation rate for this $\widehat{q_{\mathrm{sat}}}$. While the largest contributions come from near critical, values below or above critical still contribute substantially. The relatively linear range in Fig. 9b appears to suggest that a $P^{-1}e^{-\beta P}$ dependence with $\beta \sim 0.16\,(\mathrm{mm\,h^{-1}})^{-1}$ might be a reasonable approximation for moderate to high precipitation for a wide range of CWV. In both Figs. 9b and 9c, the value of P at which the precipitation contribution is a maximum moves toward higher P as CWV increases.

Overall, the distributions of precipitation discussed in this section underline the importance of considering the dependence of the precipitation PDF on where the CWV–temperature environment is relative to critical, rather than as a single PDF for total precipitation.

7. Summary and discussion

In this work, the convective transition statistics over tropical oceans are compiled using satellite retrievals and ARM site measurements to quantify the dependence of

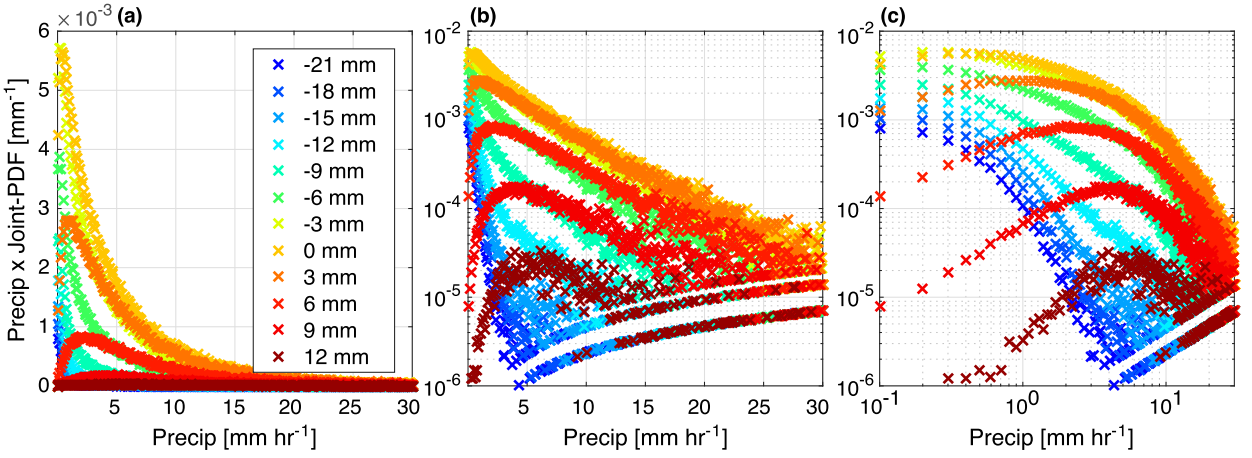

FIG. 9. Precipitation-rate-weighted joint PDF of CWV relative to critical and precipitation rate P, that is, the precipitation contribution as a function of CWV and P, for the 70-mm $\widehat{q_{\rm sat}}$ bin in the tropical western Pacific: (a) linear axes, (b) log–linear axes, and (c) log–log axes. The data correspond to the joint PDF of CWV relative to critical and P in Fig. 7a, using PR 2A25 precipitation at 0.25°. The colors indicate the values of CWV relative to w_c.

precipitation on the water vapor and tropospheric temperature environment and to provide an observational baseline for comparison in using these statistics as model diagnostics at fast (convective) time scales.

The mean tropospheric temperature profiles conditioned on precipitation ($P > 0.25\,\mathrm{mm\,h^{-1}}$; Fig. 4) show vertically coherent structure, justifying the use of bulk tropospheric temperature measures like column-integrated saturation humidity $\widehat{q_{\rm sat}}$, mass-weighted column-averaged temperature $\hat{T}$, or other layered equivalents as the leading-order description of temperature in defining the convective transition statistics. Using these temperature measures yields quantitatively similar statistics, for example, those shown in Figs. 2 and 3, including the conditional precipitation and probability of precipitation, critical CWV w_c, and PDFs of CWV for precipitating events. However, the PDFs of CWV for all events below critical may differ significantly, reflecting the differences in the climatology of these temperature measures. Because of the narrow temperature range in the tropics, the conversion among these temperature measures can be carried out using simple linear relations found by regression.

Among the robust features of the precipitation–CWV relation is the conditional precipitation as a function of CWV and tropospheric temperature, which is insensitive to spatial resolution (Figs. 1–3) and time averaging (Fig. 6), consistent with the assertion that the autocorrelation spatial and temporal scales of CWV and temperature are much greater than that of precipitation. This is particularly useful for model comparison since model output is subject to varying spatial–temporal resolution. Because of this insensitivity, w_c and the slope α characterizing the precipitation pickup are defined through the conditional precipitation. Both w_c and α are approximately constant across ocean basins, with the latter being insensitive to temperature over the most common range in the tropics. The dependence of the precipitation–CWV relation on temperature is completely characterized by w_c in the sense that shifting CWV by w_c collapses the convective transition statistics and the joint PDFs of CWV and precipitation. The dependence of w_c on temperature is, however, not a simple relation. Convective onset occurs at higher CWV but at lower CRH with increasing temperature, as noted in Neelin et al. (2009), and is consistent with the entraining plume calculations by Sahany et al. (2012). At low temperatures, which lie along the subtropical margin of the domain, critical values could plausibly be approximated by a constant CRH within a small regime. This regime likely corresponds to the subtropical expression of midlatitude frontal systems. For the most common behavior in the tropical domain, we underline that using CRH as a variable, without separately quantifying the water vapor–temperature dependence, would yield a poor characterization of the statistics, as expected because of the dominance of conditional instability as a source of tropical convective events.

Robustness of the presented statistics to instrumentation is examined by comparing various datasets, including precipitation radar, microwave retrievals, and in situ data. A major source of uncertainty in the convective transition statistics is the measurement of CWV in the presence of precipitation. Sensitivity to CWV gap filling is quantified, which primarily affects probability distributions at very high CWV (above critical). Despite the differences in

precipitation distribution, especially at high rain rate, associated with different datasets as indicated by the joint PDFs (Figs. 7, 8), both conditional precipitation and probability of precipitation are robust to instrumentation (including ground-based measurements of the former; Fig. 3). This consistency likely reflects the calibration among precipitation datasets and emphasizes the reliability of these statistics as observational references for model diagnostics.

At the time scale of the individual retrieval, the tendency of precipitation to coincide with high CWV has been observed. Here, this is quantified more precisely by including the dependence on tropospheric temperature. Specifically, CWV relative to critical (CWV $- w_c$) appears to be a useful predictor of precipitation over tropical oceans. Unlike the climatology of precipitation or CWV that shows sharp contrast between major convergence zones and regions elsewhere, the conditional probability of precipitation given CWV exceeding critical shows only minor geographic variations (Fig. 5). In other words, the convective transition statistics created from individual convective events conditioned on two bulk measures of the temperature–water vapor environment apply reasonably universally through the tropics even at the individual space–time point. Small departures are noted that are presumably due to other vertical degrees of freedom impacting convection. At larger spatial scales and subdaily time scales, events of high CWV relative to critical are almost certainly associated with convection, leading to a potential application of using CWV above critical as a precipitation predictor. A connection between above-critical events and mesoscale convective systems [Fig. 5e vs Fig. 7 of Tao and Moncrieff (2009)] is noted, which could contribute to the robustness of conditional precipitation to spatial resolution (up to ~1°). A recent analysis of the GOAmazon campaign data also points to the potential importance of organized flow in creating the dependence of deep convection on lower-tropospheric water vapor through a deep layer (Schiro et al. 2018) that is seen here as the CWV dependence of precipitation.

It is common to discuss probability distributions of precipitation and to compare models to these (e.g., Figs. 8 and 13 in Klingaman et al. 2017). However, the strong dependence of the statistics on CWV relative to critical suggests that much of the important dynamics depend on the temperature–water vapor environment of the precipitating system. We extend the scope of the precipitation–CWV relation to include the joint PDF of CWV relative to critical and precipitation rate P. This joint PDF is quantitatively similar in the most common temperature range across tropical ocean basins. For low CWV (relative to critical) the PDF drops rapidly as P increases. As CWV increases, the PDF extends into high-precipitation regime and develops a peak at a nonzero P (~3 mm h^{-1}) for the highest CWV (Fig. 7a), with most of the precipitation contribution from CWV around and above critical (mostly $P < 10$ mm h^{-1}; Fig. 9a).

Examination of the precipitation contributions suggests that the conditional distribution of precipitation in the PR 2A25 data can be approximated by the functional form $P^{-1}e^{-\beta P}$ with $\beta \sim 0.16$ (mm h^{-1})$^{-1}$ for sufficiently high P, for a wide range of CWV (Fig. 9b). This would correspond to a gamma distribution at the limit of its range of validity, except that there is a clear low-precipitation cutoff in the precipitation contribution that changes systematically as a function of CWV above critical. This apparently simple observational relationship in precipitation distributions as a function of CWV relative to critical can potentially provide an interesting target for theoretical work.

The joint PDF does exhibit dependence on spatial averaging, with the joint PDF exhibiting more light precipitation at the expense of nonprecipitating and heavily precipitating events, at lower spatial resolution (Fig. 8). This resolution dependence results in the dependence of conditional probability of precipitation on resolution, as in Figs. 1–3. There is not enough observational data to compile the joint PDF at resolutions most common for current models (~1°) without losing information for the highest CWV, but qualitative dependence of the joint PDF on distance above critical can be used as an auxiliary diagnostic tool for the evaluation of modeled convective parameterizations.

Overall, in addition to providing an observational baseline with quantified robustness and resolution dependence of the basic convective transition statistics for model comparison, the ability to summarize statistics in terms of CWV relative to critical enables additional diagnostics. The dependence of precipitation probability on this quantity expands the set of related properties that exhibit common behavior for precipitation throughout the tropics.

Acknowledgments. This research was supported by National Oceanic and Atmospheric Administration Grants NA15OAR4310097 and NA14OAR4310274, the Office of Biological and Environmental Research of the U.S. Department of Energy Grant DE-SC0011074, and National Science Foundation Grant AGS-1540518. U.S. Department of Energy Atmospheric Radiation Measurement (ARM) Climate Research Facility GOAmazon and tropical western Pacific field campaign data are acknowledged. We thank J. Meyerson for

graphical assistance. A portion of this work has previously been presented at an American Geophysical Union meeting (Kuo et al. 2016). The authors thank Dr. M. W. Moncrieff and an anonymous reviewer for insightful review comments.

REFERENCES

Ahmed, F., and C. Schumacher, 2017: Geographical differences in the tropical precipitation-moisture relationship and rain intensity onset. *Geophys. Res. Lett.*, **44**, 1114–1122, https://doi.org/10.1002/2016GL071980.

Benedict, J. J., E. D. Maloney, A. H. Sobel, D. M. W. Frierson, and L. J. Donner, 2013: Tropical intraseasonal variability in version 3 of the GFDL atmosphere model. *J. Climate*, **26**, 426–449, https://doi.org/10.1175/JCLI-D-12-00103.1.

——, ——, ——, and ——, 2014: Gross moist stability and MJO simulation skill in three full-physics GCMs. *J. Atmos. Sci.*, **71**, 3327–3349, https://doi.org/10.1175/JAS-D-13-0240.1.

Bergemann, M., and C. Jakob, 2016: How important is tropospheric humidity for coastal rainfall in the tropics? *Geophys. Res. Lett.*, **43**, 5860–5868, https://doi.org/10.1002/2016GL069255.

Bernstein, D. N., and J. D. Neelin, 2016: Identifying sensitive ranges in global warming precipitation change dependence on convective parameters. *Geophys. Res. Lett.*, **43**, 5841–5850, https://doi.org/10.1002/2016GL069022.

Booth, J. F., Y.-O. Kwon, S. Ko, R. J. Small, and R. Msadek, 2017: Spatial patterns and intensity of the surface storm tracks in CMIP5 models. *J. Climate*, **30**, 4965–4981, https://doi.org/10.1175/JCLI-D-16-0228.1.

Boyle, J. S., S. A. Klein, D. D. Lucas, H.-Y. Ma, J. Tannahill, and S. Xie, 2015: The parametric sensitivity of CAM5's MJO. *J. Geophys. Res. Atmos.*, **120**, 1424–1444, https://doi.org/10.1002/2014JD022507.

Bretherton, C. S., M. E. Peters, and L. E. Back, 2004: Relationships between water vapor path and precipitation over the tropical oceans. *J. Climate*, **17**, 1517–1528, https://doi.org/10.1175/1520-0442(2004)017<1517:RBWVPA>2.0.CO;2.

Brown, R. G., and C. Zhang, 1997: Variability of midtropospheric moisture and its effect on cloud-top height distribution during TOGA COARE. *J. Atmos. Sci.*, **54**, 2760–2774, https://doi.org/10.1175/1520-0469(1997)054<2760:VOMMAI>2.0.CO;2.

Camargo, S. J., M. K. Tippett, A. H. Sobel, G. A. Vecchi, and M. Zhao, 2014: Testing the performance of tropical cyclone genesis indices in future climates using the HiRAM model. *J. Climate*, **27**, 9171–9196, https://doi.org/10.1175/JCLI-D-13-00505.1.

Chen, D., and A. Dai, 2018: Dependence of estimated precipitation frequency and intensity on data resolution. *Climate Dyn.*, **50**, 3625–3647, https://doi.org/10.1007/s00382-017-3830-7.

Chen, Y., E. E. Ebert, K. J. E. Walsh, and N. E. Davidson, 2013: Evaluation of TRMM 3B42 precipitation estimates of tropical cyclone rainfall using PACRAIN data. *J. Geophys. Res. Atmos.*, **118**, 2184–2196, https://doi.org/10.1002/jgrd.50250.

Covey, C., P. J. Gleckler, C. Doutriaux, D. N. Williams, A. Dai, J. Fasullo, K. Trenberth, and A. Berg, 2016: Metrics for the diurnal cycle of precipitation: Toward routine benchmarks for climate models. *J. Climate*, **29**, 4461–4471, https://doi.org/10.1175/JCLI-D-15-0664.1.

Derbyshire, S. H., I. Beau, P. Bechtold, J. Y. Grandpeix, J. M. Piriou, J. L. Redelsperger, and P. M. M. Soares, 2004: Sensitivity of moist convection to environmental humidity. *Quart. J. Roy. Meteor. Soc.*, **130**, 3055–3079, https://doi.org/10.1256/qj.03.130.

Gaustad, K., and L. Riihimaki, 1996: MWR Retrievals (MWRRET1LILJCLOU), 1998-01-01 to 2010-12-31, Tropical Western Pacific (TWP) Central Facility, Manus I., PNG (C1) (updated hourly). ARM Climate Research Facility Data Archive, accessed 2016, https://doi.org/10.5439/1027369.

——, and ——, 1998: MWR Retrievals (MWRRET1LILJCLOU), 1999-01-01 to 2008-12-31, Tropical Western Pacific (TWP) Central Facility, Nauru Island (C2) (updated hourly). ARM Climate Research Facility Data Archive, accessed 2016, https://doi.org/10.5439/1027369.

——, and ——, 2015: MWR Retrievals (MWRRET1LILJCLOU), 2014-01-10 to 2015-10-20, ARM Mobile Facility (MAO) Manacapuru, Amazonas, Brazil, AMF1 (M1) (updated hourly). ARM Climate Research Facility Data Archive, accessed 2016, https://doi.org/10.5439/1027369.

Gonzalez, A., and X. Jiang, 2017: Winter mean lower-tropospheric moisture over the Maritime Continent as a climate model diagnostic metric for the propagation of the Madden-Julian oscillation. *Geophys. Res. Lett.*, **44**, 2588–2596, https://doi.org/10.1002/2016GL072430.

Hirota, H., Y. N. Takayabu, M. Watanabe, M. Kimoto, and M. Chikira, 2014: Role of convective entrainment in spatial distributions of and temporal variations in precipitation over tropical oceans. *J. Climate*, **27**, 8707–8723, https://doi.org/10.1175/JCLI-D-13-00701.1.

Holdridge, D., and J. Kyrouac, 1997: Surface Meteorological Instrumentation (MET), 1998-01-01 to 2010-12-31, Tropical Western Pacific (TWP) Central Facility, Manus I., PNG (C1) (updated hourly). ARM Climate Research Facility Data Archive, accessed 2016, https://doi.org/10.5439/1025220.

——, and ——, 1998: Surface Meteorological Instrumentation (MET), 1999-01-01 to 2008-12-31, Tropical Western Pacific (TWP) Central Facility, Nauru Island (C2) (updated hourly). ARM Climate Research Facility Data Archive, accessed 2016, https://doi.org/10.5439/1025220.

Holloway, C. E., and J. D. Neelin, 2007: The convective cold top and quasi equilibrium. *J. Atmos. Sci.*, **64**, 1467–1487, https://doi.org/10.1175/JAS3907.1.

——, and ——, 2009: Moisture vertical structure, column water vapor, and tropical deep convection. *J. Atmos. Sci.*, **66**, 1665–1683, https://doi.org/10.1175/2008JAS2806.1.

Jiang, X., 2017: Key processes for the eastward propagation of the Madden-Julian oscillation based on multi-model simulations. *J. Geophys. Res. Atmos.*, **122**, 755–770, https://doi.org/10.1002/2016JD025955.

——, M. Zhao, E. Maloney, and D. E. Waliser, 2016: Convective moisture adjustment time-scale as a key factor in regulating model amplitude of the Madden-Julian oscillation. *Geophys. Res. Lett.*, **43**, 10 412–10 419, https://doi.org/10.1002/2016GL070898.

Kanamitsu, M., W. Ebisuzaki, J. Woollen, S. Yang, J.J. Hnilo, M. Fiorino, and G.L. Potter, 2002: NCEP–DOE AMIP-II Reanalysis (R-2). *Bull. Amer. Meteor. Soc.*, **83**, 1631–1643, https://doi.org/10.1175/BAMS-83-11-1631.

Kim, D., and Coauthors, 2014: Process-oriented MJO simulation diagnostic: Moisture sensitivity of simulated convection. *J. Climate*, **27**, 5379–5395, https://doi.org/10.1175/JCLI-D-13-00497.1.

Klingaman, N. P., G. M. Martin, and A. Moise, 2017: ASoP (v1.0): A set of methods for analyzing scales of precipitation in general circulation models. *Geosci. Model Dev.*, **10**, 57–83, https://doi.org/10.5194/gmd-10-57-2017.

Koontz, A., J. Kyrouac, and S. Springston, 2015: Aerosol Observing System meteorological data (AOSMET), 2014-01-10 to 2015-10-20, ARM Mobile Facility (MAO) Manacapuru, Amazonas, Brazil, MAOS (S1) (updated hourly). ARM Climate Research Facility Data Archive, accessed 2016, https://doi.org/10.5439/1025153.

Kuo, Y.-H., and Coauthors, 2016: Convective transition statistics for climate model diagnostics. *2016 Fall Meeting*, San Francisco, CA, Amer. Geophys. Union, Abstract A13L-03.

——, J. D. Neelin, and C. R. Mechoso, 2017: Tropical convective transition statistics and causality in the water vapor–precipitation relation. *J. Atmos. Sci.*, **74**, 915–931, https://doi.org/10.1175/JAS-D-16-0182.1.

Langenbrunner, B., and J. D. Neelin, 2017: Multiobjective constraints for climate model parameter choices: Pragmatic Pareto fronts in CESM1. *J. Adv. Model. Earth Syst.*, **9**, 2008–2026, https://doi.org/10.1002/2017MS000942.

Lin, J. W.-B., and J. D. Neelin, 2003: Toward stochastic deep convective parameterization in general circulation models. *Geophys. Res. Lett.*, **30**, 1162, https://doi.org/10.1029/2002GL016203.

Mapes, B., and R. Neale, 2011: Parameterizing convective organization to escape the entrainment dilemma. *J. Adv. Model. Earth Syst.*, **3**, M06004, https://doi.org/10.1029/2011MS000042.

——, S. Tulich, J. Lin, and P. Zuidema, 2006: The mesoscale convection life cycle: Building block or prototype for largescale tropical waves? *Dyn. Atmos. Oceans*, **42**, 3–29, https://doi.org/10.1016/j.dynatmoce.2006.03.003.

Moncrieff, M. W., C. Liu, and P. Bogenschutz, 2017: Simulation, modeling, and dynamically based parameterization of organized tropical convection for global climate models. *J. Atmos. Sci.*, **74**, 1363–1380, https://doi.org/10.1175/JAS-D-16-0166.1.

Muller, C. J., L. E. Back, P. A. O'Gorman, and K. A. Emanuel, 2009: A model for the relationship between tropical precipitation and column water vapor. *Geophys. Res. Lett.*, **36**, L16804, https://doi.org/10.1029/2009GL039667.

Neelin, J. D., O. Peters, J. W.-B. Lin, K. Hales, and C. E. Holloway, 2008: Rethinking convective quasi-equilibrium: Observational constraints for stochastic convective schemes in climate models. *Philos. Trans. Roy. Soc. London*, **366A**, 2581–2604, https://doi.org/10.1098/rsta.2008.0056.

——, ——, and K. Hales, 2009: The transition to strong convection. *J. Atmos. Sci.*, **66**, 2367–2384, https://doi.org/10.1175/2009JAS2962.1.

Oueslati, B., and G. Bellon, 2013: Convective entrainment and large-scale organization of tropical precipitation: Sensitivity of the CNRM-CM5 hierarchy of models. *J. Climate*, **26**, 2931–2946, https://doi.org/10.1175/JCLI-D-12-00314.1.

Parsons, D. B., J.-L. Redelsperger, and K. Yoneyama, 2000: The evolution of the tropical western Pacific atmosphere-ocean system following the arrival of a dry intrusion. *Quart. J. Roy. Meteor. Soc.*, **126**, 517–548, https://doi.org/10.1002/qj.49712656307.

Peters, O., and J. D. Neelin, 2006: Critical phenomena in atmospheric precipitation. *Nat. Phys.*, **2**, 393–396, https://doi.org/10.1038/nphys314.

Redelsperger, J. L., D. B. Parsons, and F. Guichard, 2002: Recovery processes and factors limiting cloud-top height following the arrival of a dry intrusion observed during TOGA COARE. *J. Atmos. Sci.*, **59**, 2438–2457, https://doi.org/10.1175/1520-0469(2002)059<2438:RPAFLC>2.0.CO;2.

Ridout, J. A., 2002: Sensitivity of tropical Pacific convection to dry layers at mid- to upper levels: Simulation and parameterization tests. *J. Atmos. Sci.*, **59**, 3362–3381, https://doi.org/10.1175/1520-0469(2002)059<3362:SOTPCT>2.0.CO;2.

Rowell, D. P., 2012: Sources of uncertainty in future changes in local precipitation. *Climate Dyn.*, **39**, 1929–1950, https://doi.org/10.1007/s00382-011-1210-2.

Rushley, S. S., D. Kim, C. S. Bretherton, and M.-S. Ahn, 2018: Reexamining the nonlinear moisture-precipitation relationship over the tropical oceans. *Geophys. Res. Lett.*, **45**, 1133–1140, https://doi.org/10.1002/2017GL076296.

Sahany, S., J. D. Neelin, K. Hales, and R. B. Neale, 2012: Temperature–moisture dependence of the deep convective transition as a constraint on entrainment in climate models. *J. Atmos. Sci.*, **69**, 1340–1358, https://doi.org/10.1175/JAS-D-11-0164.1.

——, ——, ——, and ——, 2014: Deep convective transition characteristics in the Community Climate System Model and changes under global warming. *J. Climate*, **27**, 9214–9232, https://doi.org/10.1175/JCLI-D-13-00747.1.

Sanderson, B. M., 2011: A multimodel study of parametric uncertainty in predictions of climate response to rising greenhouse gas concentrations. *J. Climate*, **24**, 1362–1377, https://doi.org/10.1175/2010JCLI3498.1.

Schiro, K. A., J. D. Neelin, D. K. Adams, and B. R. Lintner, 2016: Deep convection and column water vapor over tropical land versus tropical ocean: A comparison between the Amazon and the tropical western Pacific. *J. Atmos. Sci.*, **73**, 4043–4063, https://doi.org/10.1175/JAS-D-16-0119.1.

——, F. Ahmed, S. E. Giangrande, and J. D. Neelin, 2018: GoAmazon2014/5 campaign points to deep-inflow approach to deep convection across scales. *Proc. Natl. Acad. Sci. USA*, https://doi.org/10.1073/pnas.1719842115, in press.

Sherwood, S. C., and R. Wahrlich, 1999: Observed evolution of tropical deep convective events and their environment. *Mon. Wea. Rev.*, **127**, 1777–1795, https://doi.org/10.1175/1520-0493(1999)127<1777:OEOTDC>2.0.CO;2.

——, S. Bony, and J.-L. Dufresne, 2014: Spread in model climate sensitivity traced to atmospheric convective mixing. *Nature*, **505**, 37–42, https://doi.org/10.1038/nature12829.

Stechmann, S. N., and J. D. Neelin, 2011: A stochastic model for the transition to strong convection. *J. Atmos. Sci.*, **68**, 2955–2970, https://doi.org/10.1175/JAS-D-11-028.1.

——, and ——, 2014: First-passage-time prototypes for precipitation statistics. *J. Atmos. Sci.*, **71**, 3269–3291, https://doi.org/10.1175/JAS-D-13-0268.1.

Tao, W.-K., and M. W. Moncrieff, 2009: Multiscale cloud system modeling. *Rev. Geophys.*, **47**, RG4002, https://doi.org/10.1029/2008RG000276.

Tompkins, A. M., 2001: Organization of tropical convection in low vertical wind shears: The role of water vapor. *J. Atmos. Sci.*, **58**, 529–545, https://doi.org/10.1175/1520-0469(2001)058<0529:OOTCIL>2.0.CO;2.

Torri, G., Z. Kuang, and Y. Tian, 2015: Mechanisms for convection triggering by cold pools. *Geophys. Res. Lett.*, **42**, 1943–1950, https://doi.org/10.1002/2015GL063227.

TRMM, 2011a: TRMM Precipitation Radar rainfall rate and profile L2 1.5 hours V7. Goddard Earth Sciences Data and Information Services Center, accessed 19 August 2016, https://disc.gsfc.nasa.gov/datacollection/TRMM_2A25_7.html.

——, 2011b: TRMM (TMPA) rainfall estimate L3 3 hour 0.25 degree × 0.25 degree V7. Goddard Earth Sciences Data and Information Services Center, accessed 8 July 2016, https://disc.gsfc.nasa.gov/datacollection/TRMM_3B42_7.html.

University of Wyoming, 2017: Atmospheric soundings. Dept. of Atmospheric Sciences, University of Wyoming, accessed 21 August 2017, http://weather.uwyo.edu/upperair/sounding.html.

Wentz, F. J., C. Gentemann, and K. A. Hilburn, 2015: Remote Sensing Systems TRMM TMI Daily Environmental Suite on 0.25 deg grid, version 7.1. Remote Sensing Systems, accessed 8 July 2016, www.remss.com/missions/tmi.

Yano, J.-I., C. Liu, and M. W. Moncrieff, 2012: Self-organized criticality and homeostasis in atmospheric convective organization. *J. Atmos. Sci.*, **69**, 3449–3462, https://doi.org/10.1175/JAS-D-12-069.1.

Yokohata, T., J. D. Annan, M. Collins, C. S. Jackson, M. Tobis, M. Webb, and J. C. Hargreaves, 2012: Reliability of multi-model and structurally different single-model ensembles. *Climate Dyn.*, **39**, 599–616, https://doi.org/10.1007/s00382-011-1203-1.